JOURNAL OF GEOPHYSICAL RESEARCH, VOL. 100, NO. D8, PAGES 16,491–16,505, AUGUST 20, 1995

Trajectory mapping and applications to data from the Upper Atmosphere Research Satellite

Gary A. Morris,[1,2] Mark R. Schoeberl,[3] Lynn C. Sparling,[4] Paul A. Newman,[3] Leslie R. Lait,[4] Lee Elson,[5] Joe Waters,[5] Robert A. Suttie,[6] Aidan Roche,[7] Jack Kumer,[7] and James M. Russell, III[8]

Abstract. The problem of creating synoptic maps from asynoptically gathered trace gas data has prompted the development of a number of schemes. Most notable among these schemes are the Kalman filter, the Salby–Fourier technique, and constituent reconstruction. This paper explores a new technique called "trajectory mapping." Trajectory mapping creates synoptic maps from asynoptically gathered data by advecting measurements backward or forward in time using analyzed wind fields. A significant portion of this work is devoted to an analysis of errors in synoptic trajectory maps associated with the calculation of individual parcel trajectories. In particular, we have considered (1) calculational errors; (2) uncertainties in the values and locations of constituent measurements, (3) errors incurred by neglecting diabatic effects, and (4) sensitivity to differences in wind field analyses. These studies reveal that the global fields derived from the advection of large numbers of measurements are relatively insensitive to the errors in the individual trajectories. The trajectory mapping technique has been successfully applied to a variety of problems. In this paper, the following two applications demonstrate the usefulness of the technique: an analysis of dynamical wave–breaking events and an examination of Upper Atmosphere Research Satellite data accuracy.

1. Introduction

A fundamental problem in observing systems is the generation of synoptic maps from asynoptically gathered data. Kalman filtering [*Haggard* et al. 1986] and the Salby–Fourier transform method [*Salby*, 1982 a,b; *Lait and Stanford*, 1988] use asynoptic data to construct synoptic maps. These methods have been successfully applied to Nimbus 7 limb infrared monitor of the stratosphere (LIMS) data [*Remsberg et al.* 1984] and Upper Atmosphere Research Satellite (UARS) data [*Elson and Froidevaux*, 1993]. Both of these methods employ strictly mathematical techniques to produce synoptic maps of any meteorological variable or trace gas field with a sufficiently long, continuous series of measurements.

The use of available ancillary information, such as analyzed meteorological data, however, can provide a powerful constraint on trace gas observations. The constituent reconstruction technique described by *Schoeberl et al.* [1989] and *Schoeberl and Lait* [1992], for example, can generate synoptic maps from data sets of almost any size. By requiring that long–lived trace gas isopleths be aligned with potential temperature and potential vorticity (PV) contours over the sampling period, the technique is able to provide estimates of the field, even in regions remote from measurements. The reconstruction technique works best for trace gases in near equilibrium with the flow field (i.e., regions where the trace gas variance along the PV contour is small, as is usually the case with long–lived trace gases) but is inappropriate for released or short–lived trace gases.

This paper describes trajectory mapping, which, like reconstruction, utilizes meteorological information to create synoptic maps. *Pierce et al.* [1994] first employed such a technique to create synoptic maps from Halogen Occultation Experiment (HALOE) data. Unlike reconstruction, the trajectory mapping technique makes few assumptions about atmospheric mixing.

After providing a brief description of the trajectory mapping technique, we demonstrate its effectiveness through applications to UARS data. First, we gen-

[1]Dept. of Space Physics and Astronomy, Rice University, Houston, Texas.
[2]Now at NASA Goddard Space Flight Center, Greenbelt, Maryland.
[3]NASA Goddard Space Flight Center, Greenbelt, Maryland.
[4]Hughes STX Corporation, Lanham, Maryland.
[5]Jet Propulsion Laboratory, California Institute of Technology, Pasadena, California.
[6]Heriot–Watt University, Edinburgh, Scotland.
[7]Lockheed Palo Alto Research Laboratory, Palo Alto, California.
[8]NASA Langley Research Center, Hampton, Virginia.

Paper number 95JD01072.
0148-0227/95/95JD-01072$05.00

erate and compare maps of identical data sets from the cryogenic limb array etalon spectrometer (CLAES) using the Salby–Fourier, Kalman filtering, and trajectory mapping techniques. We then use trajectory maps to study the evolution of atmospheric wave–breaking events. Next, we evaluate the reliability of trajectory mapping by examining the following four potential error sources: computational error, measurement uncertainties, the isentropic approximation, and differences in meteorological analyses. These error studies reveal that the quality of most measurements advected with the trajectory model remains high over periods of at least several days, while the quality of the fields produced from the advection of a large ensemble of measurements remains high for much longer periods. Finally, a comparison of microwave limb sounder (MLS) and HALOE water vapor data demonstrates one possible application of the technique.

2. The Trajectory Mapping Technique

The trajectory mapping technique combines several of the strengths of previous techniques with a minimum of assumptions. Trajectory mapping employs a simple, two–dimensional model of atmospheric motions (known as the trajectory model) to advect measurements forward or backward in time from the point at which they were made. Meteorological analyses provide the winds which determine the magnitude and direction of parcel motion at each time step. The trajectory technique constructs its synoptic maps by advecting a large number of measurements (all made at different times) to the same instant in time. These maps are known as "trajectory maps."

Unlike Kalman filtering [*Haggard et al.*, 1986], trajectory mapping does not require knowledge of the error associated with each measurement. Knowing these errors, however, is helpful in assessing the validity of trajectory maps. Since both measurement and meteorological errors are present in trajectory mapping, determining the actual errors associated with trajectory maps can be quite complicated (see section 4).

The trajectory mapping technique is relatively unaffected by missing data points or periods of satellite data dropout, both of which can complicate the Salby–Fourier technique [*Lait and Stanford*, 1988]. Furthermore, so long as the wind field analyses exist, trajectory maps can be produced outside of periods during which the satellite measurements are made. Trajectory mapping, therefore, allows a clearer explanation of atmospheric dynamical events which occur, at least in part, outside data gathering periods (see the CLAES example in section 3).

The trajectory technique demonstrates several additional strengths. First, its synoptic maps are generated easily and straightforwardly from asynoptic data. Second, the technique allows for comparison of noncoincident or noncollocated measurements. Third, the technique makes no assumptions about the amount of mixing occurring in the real atmosphere (unlike constituent reconstruction, which assumes uniformly mixed [PV, θ] tubes). Fourth, the technique applies no artificial, mathematical constraints to the data nor does it require the binning of data in any way (unlike the Kalman filtering, Salby–Fourier, and reconstruction techniques). Fifth, the technique provides the potential to easily separate transport from chemical effects (for example, see *Manney et al.* [1995]).

The ability of synoptic mapping techniques, like trajectory mapping, to compare noncoincident and noncollocated measurements facilitates data validation studies. This paper provides an example comparing H_2O measurements from MLS and HALOE.

The trajectory mapping technique has several disadvantages as compared to other methods. First, the quality of trajectory maps is substantially dependent upon the quality of the meteorological fields. Missing or inaccurate meteorological data degrade the accuracy of the advected measurements. Constituent reconstruction is similarly dependent upon the accuracy of the meteorological fields, while Kalman filtering and the Salby–Fourier techniques rely strictly on mathematical fits to the measurements. Second, unlike the Kalman–filtered, Salby–Fourier, or reconstructed maps, the trajectory maps in this paper are not uniformly gridded. An innovative technique [*Sutton et al.*, 1994] has been recently developed, however, which produces uniformly gridded trajectory maps. Third, the application of trajectory mapping, like reconstruction, is confined to constituent data, while Kalman filtering and the Salby–Fourier technique can be applied to data sets of any type.

An understanding of the accuracy of the trajectory computation is critical to assessing the value of the resultant maps. A considerable portion of this paper, therefore, is devoted to evaluating errors associated with the technique.

3. Trajectory Mapping of Satellite Data

To illustrate the trajectory mapping technique, we used long–lived trace gas data gathered by two instruments aboard UARS. In the first example, CLAES measurements of N_2O, a long–lived, stratospheric trace gas [*Brasseur and Solomon*, 1984], are asynoptically (Plate 1a), Salby–Fourier (Plate 1b), Kalman–filtered (Plate 1c), and trajectory mapped (Plates 1d and 1e, with the latter being derived from the former using a Barnes gridding scheme, discussed further below) on September 9, 1992. The CLAES data have been interpolated to the 800 K isentropic surface. During this period in September 1992, UARS is in "forward flight" mode with CLAES viewing from 30°N to 80°S.

All of the synoptic maps (Plates 1b–1e) were produced with data gathered from September 6 through 12. To produce the trajectory maps of Plates 1d and 1e, data from September 6 through noon on September 9 were advected forward in time, while data gathered from midnight on September 13 back to noon on September 9 were advected backward in time. Bal-

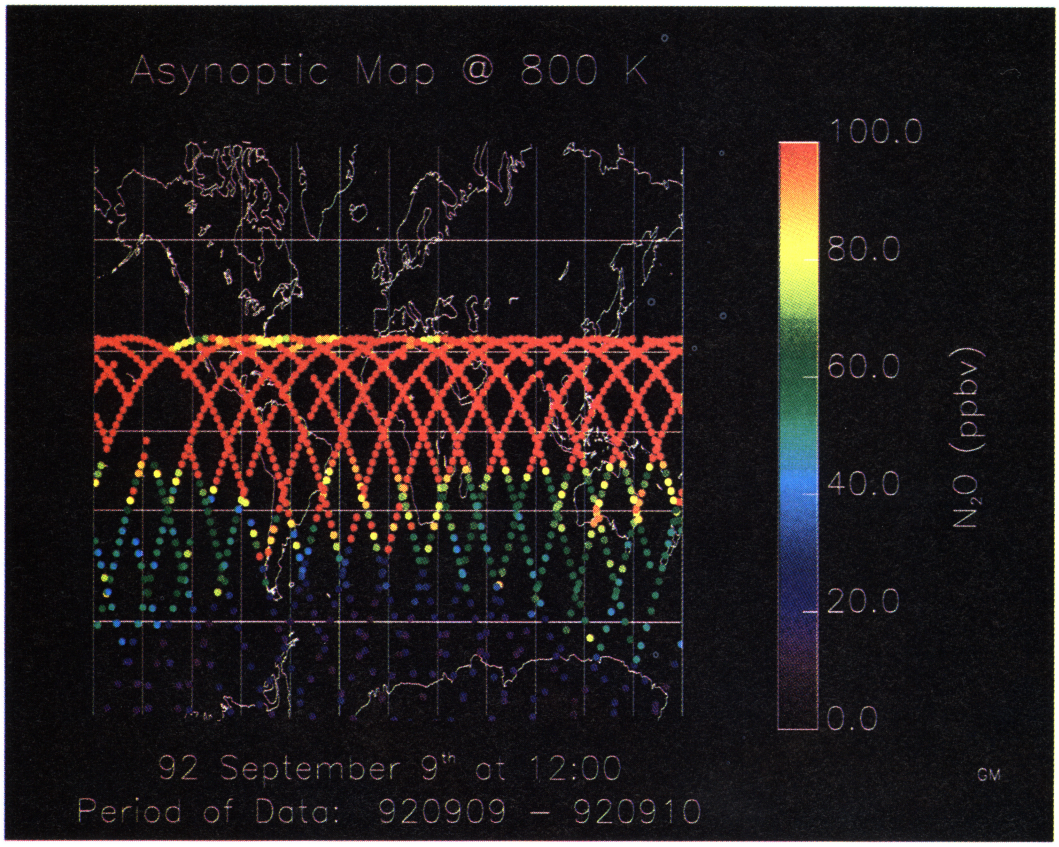

Plate 1a. An asynoptic map showing the cryogenic limb array etalon spectrometer (CLAES) data–gathering pattern for 1 day (September 9, 1992).

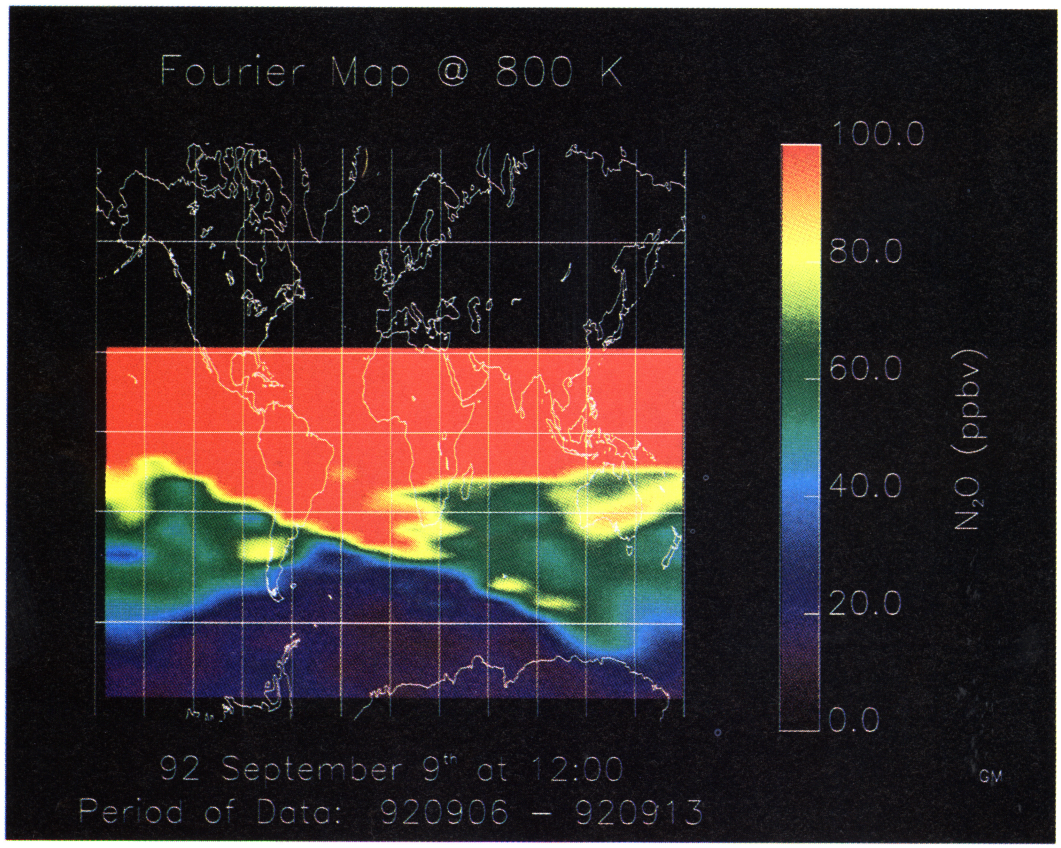

Plate 1b. Synoptic map of CLAES N_2O data at noon on September 9, 1992, on the 800 K potential temperature surface using the Salby–Fourier method.

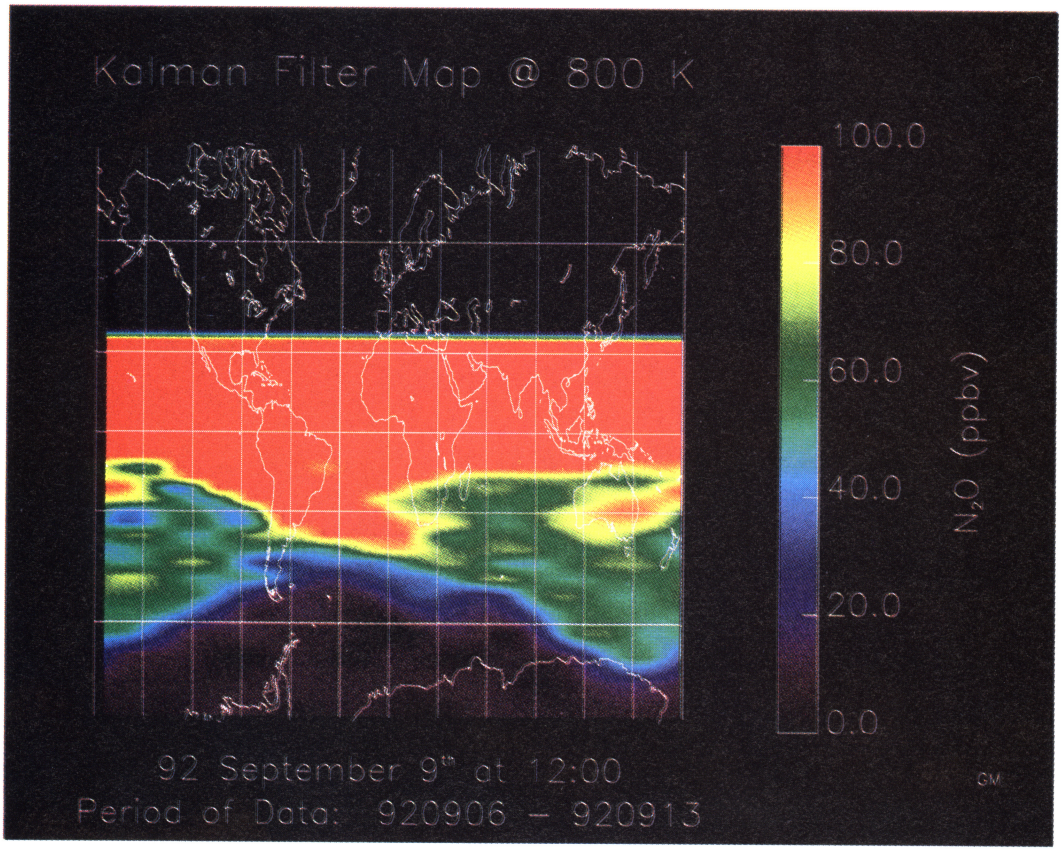

Plate 1c. Kalman–filtered map of the same data used in Plate 1b.

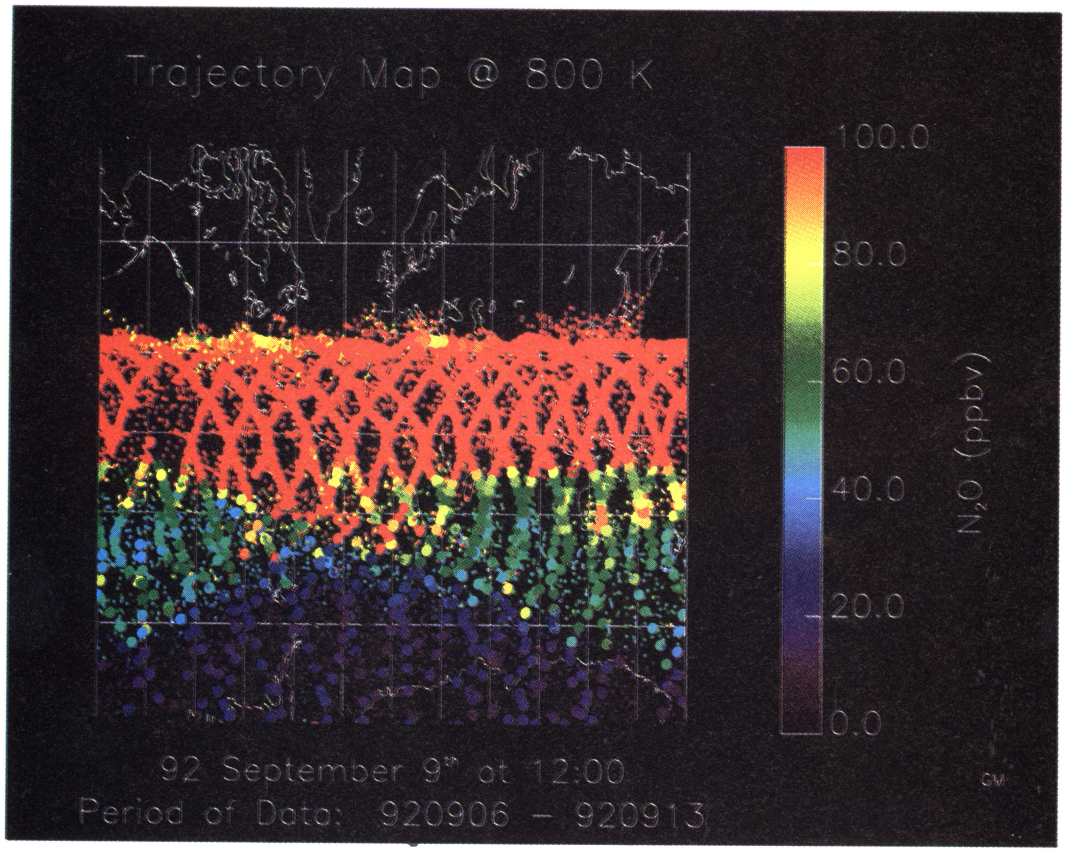

Plate 1d. Trajectory map of the same data used in Plate 1b.

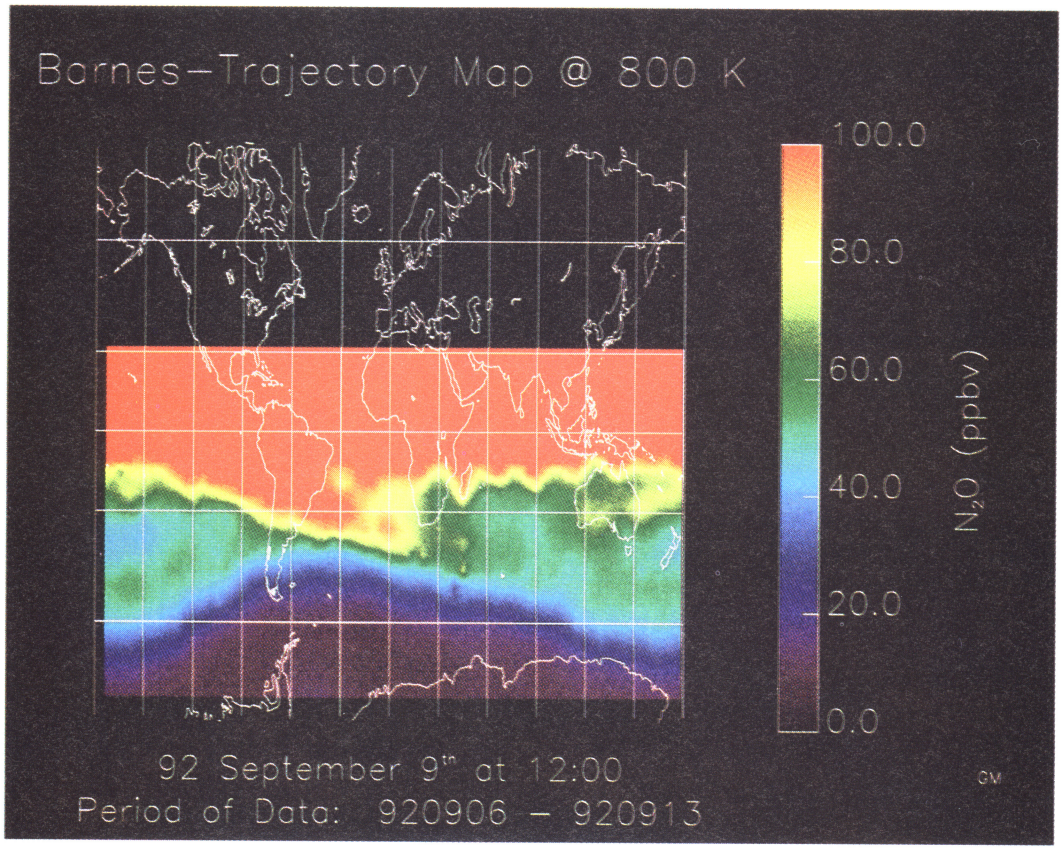

Plate 1e. Gridded trajectory map (derived from Plate 1d using a Barnes scheme).

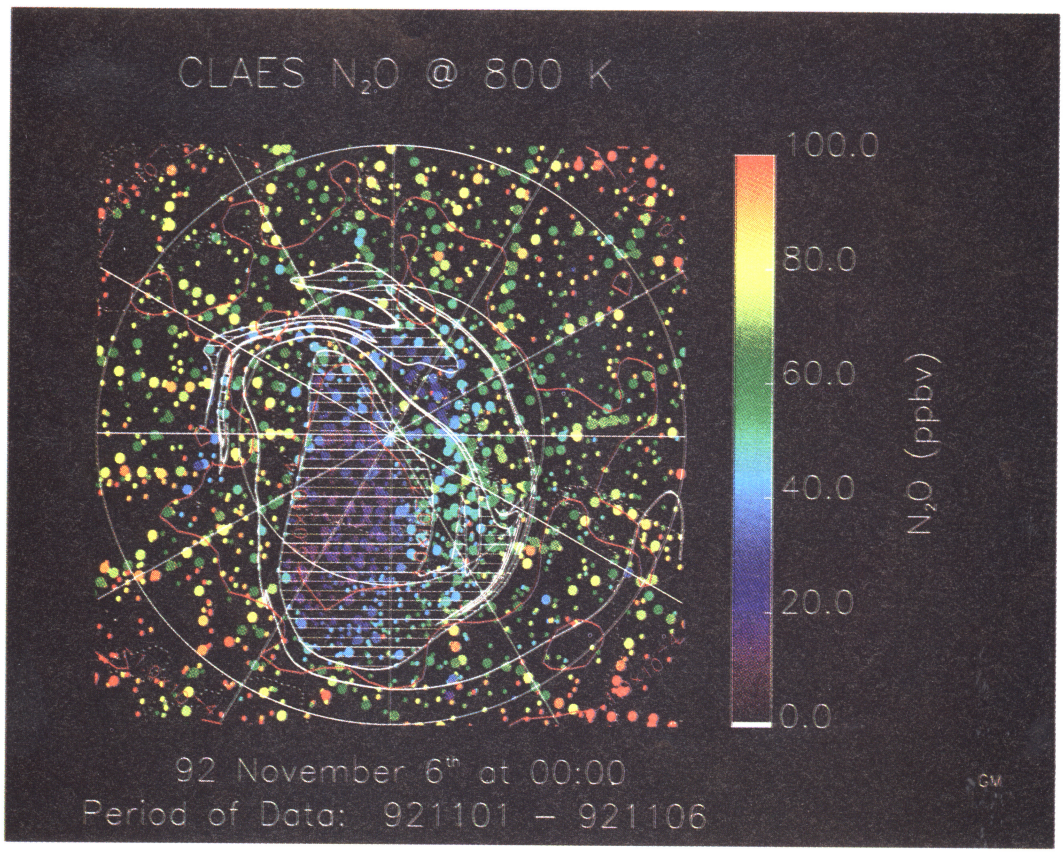

Plate 2. Trajectory map of CLAES N_2O on November 6, 1992, at 800 K. Overplotted in red are lines of constant National Meteorological Center (NMC) potential vorticity (PV). The white cross–hatched region represents the interior of the vortex, as defined by an 8 day advection of the -2.6×10^{-4} NMC PV contour. The larger dots represent data added within the most recent 24 hours, while smaller dots represent older data.

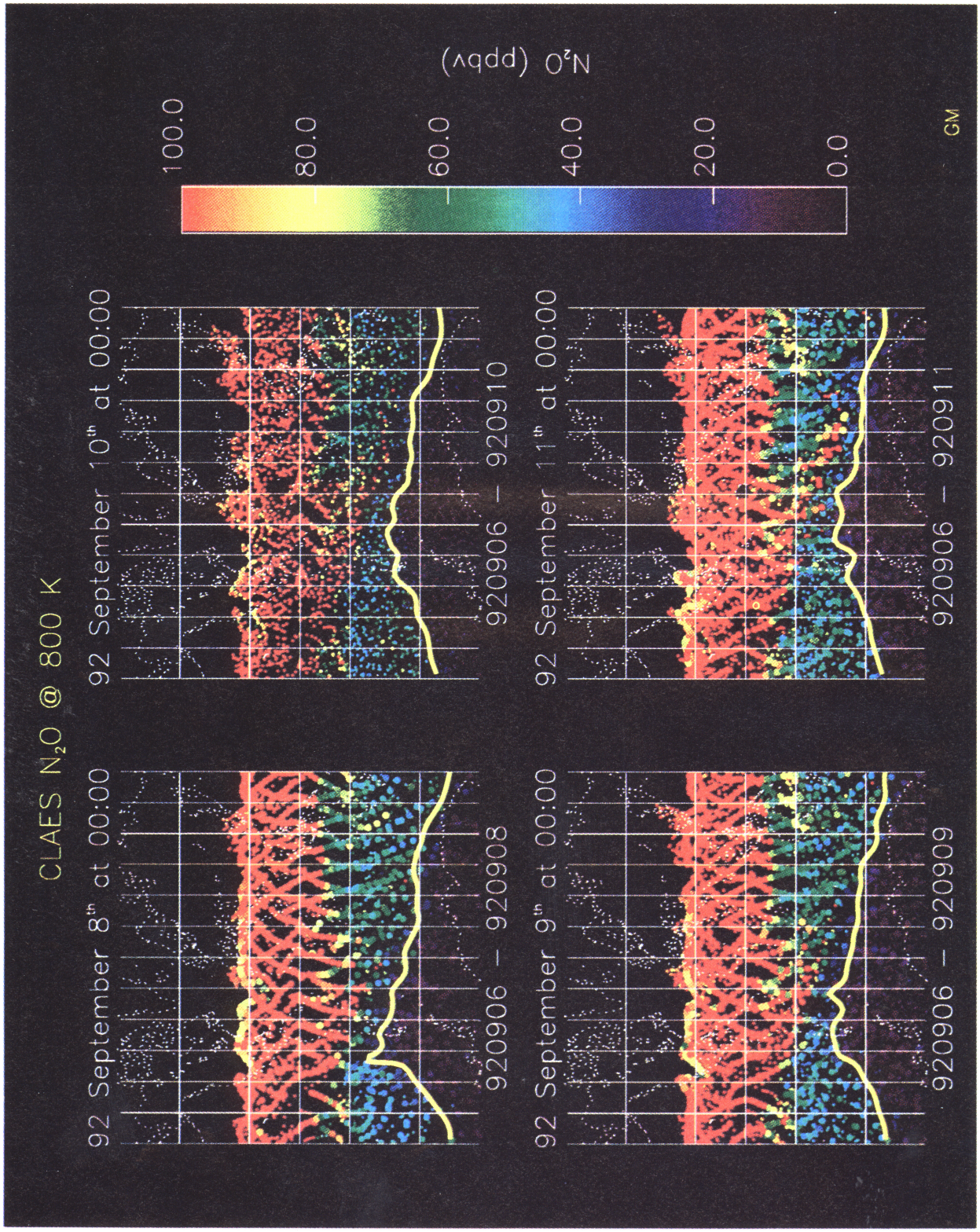

Plate 3. A series of trajectory maps of the September 1992 wave–breaking event as seen in the CLAES N_2O data at 800 K. The thick yellow line represents the edge of the vortex as defined by the -3.0×10^{-4} NMC PV contour.

anced winds derived from National Meteorological Center (NMC) temperatures and geopotential heights [*Randel*, 1987a, *Newman et al.*, 1988] were used to isentropically advect the measurements. Note that due to inaccuracies in the balanced wind approximation near the equator, parcel locations equatorward of 20° are particularly suspect.

In the trajectory map (Plate 1d) the larger dots represent parcels which have been advected by the trajectory model for periods less than 12 hours (i.e., the measurements of September 9). The smaller dots represent parcels added more than 12 hours before or after the time of the synoptic map (for this case, 1200 UT on September 9, 1992). The trajectory technique appears to preserve the large-scale distribution of N_2O, as indicated by the good agreement between the older and more recent N_2O measurements. Similarly good agreement between advected measurements and new measurements was also found in a study of HALOE data [*Pierce et al.*, 1994].

The synoptic maps of Plates 1a–1c clearly demonstrate the advantage gained by using more than 1 day of data in map production. While the single-day UARS data provide global coverage (Plate 1a), the map coverage and resolution improve dramatically when several days of data are combined through one of the synoptic techniques (Plates 1b–1e). Furthermore, the synoptic maps are all highly consistent with the satellite data.

Comparing the various gridded maps, we observe a more uniform midlatitude constituent distribution in the trajectory map (Plate 1e) than in the Salby–Fourier map (Plate 1b) or Kalman-filtered map (Plate 1c), both of which appear to contain evidence of Fourier ringing (the alternating high and low N_2O patches on a given latitude circle). In addition, the trajectory map shows smoother gradients inside the vortex and at the vortex boundary. (In part, this result is an artifact of the scheme used to produce the gridded product from the trajectory data. The Barnes scheme computes a weighted average of parcel values within 1000 km of each grid point. The weighting factor used here was inversely related to the distance of each parcel from the grid point location. Such a scheme naturally smooths out small-scale structures.)

The gridded maps, however, all contain somewhat less information than the trajectory map of Plate 1d. By depicting each measurement, the trajectory map allows an estimate of the variance through visual inspection that none of the maps of Plates 1b, 1c, or 1e allows.

Unlike the Salby–Fourier and Kalman filtering techniques, trajectory mapping can be performed without consideration of data aliasing and can frequently produce high quality maps with far less data than the 7 days used to produce Plates 1d and 1e. Seven days of data were chosen for use in the trajectory maps only so as to correspond exactly with the data used to produce the Salby–Fourier and Kalman-filtered maps of Plates 1b and 1c.

The trajectory mapping technique is also capable of reproducing small scale dynamical structures. For example, Plate 2 shows a trajectory map generated for November 6, 1992. At this time the Antarctic vortex appears to have shifted off the pole and to have shed material to midlatitudes. Low N_2O filaments (indicated by the dark blue points) can still be seen peeling off the vortex. The low N_2O values present among the higher, midlatitude values (green points) probably had their origins at or near the vortex edge.

To confirm this hypothesis, a contour advection computation described by *Schoeberl and Sparling* [1994] was used to track the vortex edge (here defined by the -2.6×10^{-4} (K m^2)(kg s)$^{-1}$ NMC PV contour) forward in time for 8 days from October 28. When advected to the time of and overlaid on the trajectory map (see Plate 2), the PV contour seems to explain much of the low N_2O air found outside the vortex (the white cross-hatched region represents vortex air). Evidence for the reality of small-scale features of the type generated in the contour advection shown here has been provided by *Waugh et al.* [1994] and *Plumb et al.* [1994]. Also noteworthy in Plate 2 is the general agreement between the N_2O gradient and the gradient in NMC PV values (red contours). Such agreement is found in nearly all maps produced by the trajectory mapping technique.

As another demonstration of trajectory mapping, Plate 3 maps the evolution of the September tropical wave-breaking event [*Randel et al.*, 1993] over the 4 days from September 8 to 11, 1992. The larger points in these maps represent data which have been added in the 24-hour period prior to the time of the synoptic map. The yellow line represents the edge of the vortex as defined by the -3.0×10^{-4} (K m^2)(kg s)$^{-1}$ NMC PV contour. As in Plate 2, the gradient in N_2O across the vortex boundary and the good agreement between new and old measurements are again well illustrated.

In order to demonstrate the technique's ability to perform despite data gaps, data from September 10 were omitted in the production of Plate 3. As can be seen, the trajectory technique successfully generated a synoptic map on that day despite the lack of data. The use of advected, older data to produce a map on September 10 completed the otherwise incomplete picture of the evolution of the event.

As a final example, Plate 4 shows the large-scale intrusion of tropical air to mid- and high northern latitudes in February 1993 (also reported by *Randel et al.* [1993] and further examined by *Manney et al.* [1994]). MLS H_2O data from February 18 to 23, 1993 are shown in Plate 4. Forward in time, isentropic trajectory maps were generated on successive days from February 20 to 23 on the 800 K isentropic surface. Like N_2O, the lifetime of H_2O at these altitudes has been shown to be sufficiently long for H_2O to be considered a valid dynamical trace gas [*Brasseur and Solomon*, 1984].

As in the previous examples, good agreement between constituent and NMC PV gradients is again evident in the MLS H_2O trajectory maps. In addition, good agreement between new measurements (larger dots) and older, advected measurements (smaller dots) again lends confidence to both the technique and the measurements.

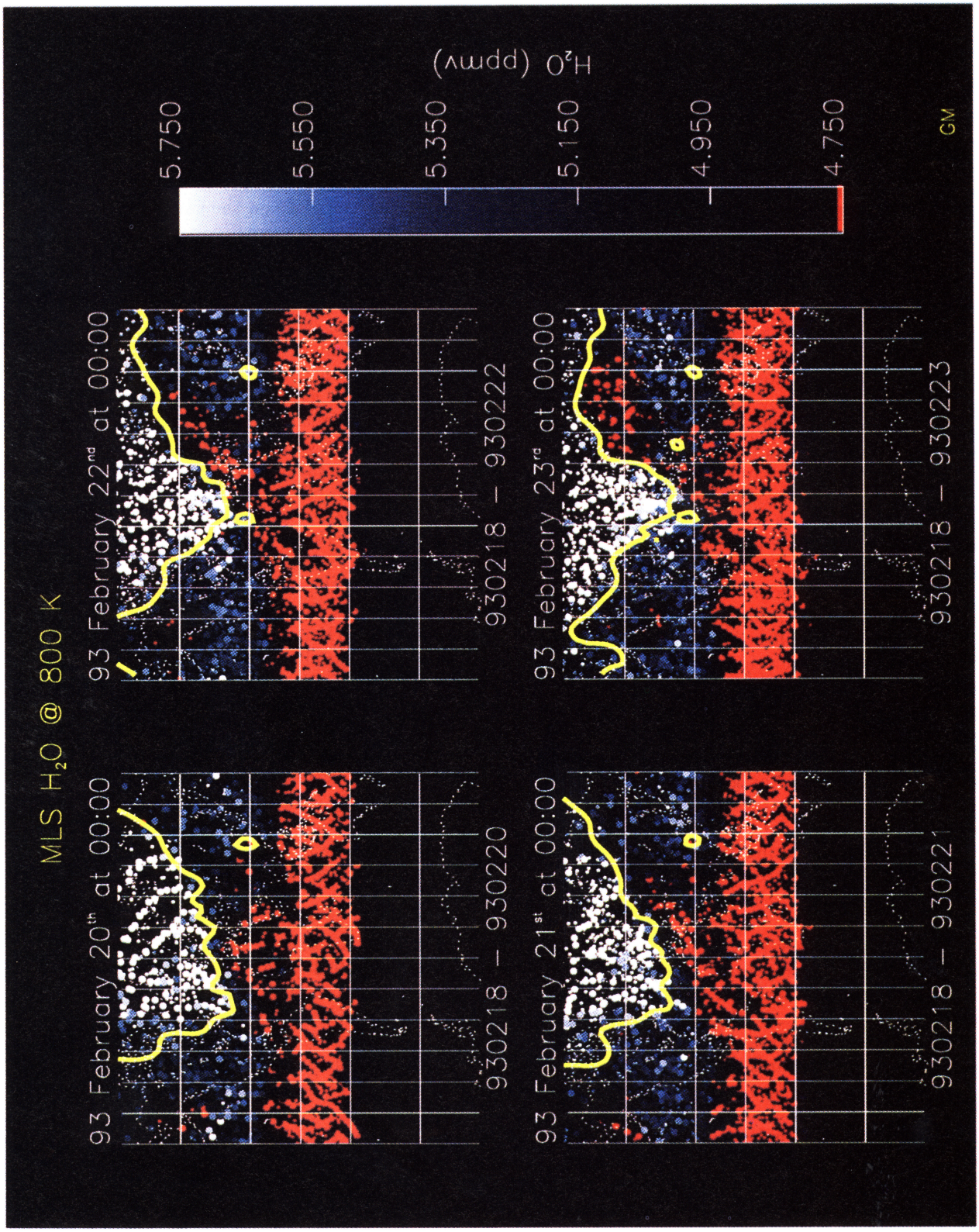

Plate 4. A series of trajectory maps of the February 1993 wave–breaking event as seen in the microwave limb sounder (MLS) H_2O data at 800 K. The thick yellow line represents the edge of the vortex as defined by the 3.0×10^{-4} NMC PV contour.

4. Errors in Trajectory Mapping

As mentioned in section 1, the validity of trajectory mapping is fundamentally dependent on the accuracy of the trajectory calculations. The information about an individual parcel location degrades with time owing to the cumulative effects of errors along its trajectory. The spatial distribution of a large ensemble of parcels, however, is less sensitive to these errors, as shown below. A fundamental problem, therefore, is to determine a reasonable upper bound for the length of time over which parcel trajectories are accurate. Another problem concerns the maximum age for which measurements included in trajectory maps can be considered valid. In exploring these problems, we shall discuss the following four potential sources of error in both individual trajectory calculations and trajectory maps: computational error, trace gas measurement uncertainties, the use of the isentropic approximation, and meteorological errors.

4.1 Computational Error

The first of these four error sources, the computational error, has been examined and found to be quite small for the fourth–order Runge–Kutta time integration scheme used here [*Schoeberl and Sparling*, 1994]. Computational error, therefore, can be ignored, especially as compared with the magnitudes of the other sources of error considered below.

4.2 Measurement Uncertainties

The second of the error sources, measurement uncertainties, consists of the following two basic components: the initial constituent measurement error and the subsequent model advection error. The former of these two errors is inherent in the measurement and remains constant with time, while the latter is a result of the trajectory calculation and grows with time.

First, consider the satellite measurement errors. Inaccurate measurement of the constituent and improper pressure registration both contribute to erroneous values. (For further discussion of these errors, see the special section on UARS in the *Journal of Geophysical Research 98(D6)*). Furthermore, the scale of the satellite footprint limits the minimum size of observable atmospheric features. The satellite can detect only those features on the order of or larger in scale than the satellite footprint. In regions with small–scale features, the agreement between recently made and older, advected satellite measurements will be diminished. Examples of this effect can be found in both Plates 2 and 3. In Plate 2 notice that the filament extending away from and around the vortex has grown very long and very thin, a process discussed by *Pierce and Fairlie* [1993]. As a result, few of the new satellite measurements around the thin filament are indicative of vortex air. In Plate 3, as the wave breaks, the tongue of high N_2O (red) material is stretched into a narrow filament. Nearby, newer satellite measurements (represented by the larger dots) begin to decrease in value with time, as compared to the older, advected measurements (represented by the smaller dots). Instrumental limitations, therefore, cause older, advected measurements (particularly those which have been pulled out in filaments) to disagree with nearby, newer measurements.

Another cause of the disagreement, however, can be found in the trajectory technique. Because these trajectory calculations are nondiffusive, they will preserve filamentary structures for longer periods of time than may be physically warranted. Hence, disagreements between new and old measurements can also be caused by model errors.

In addition to uncertainty in measured constituent mixing ratios, uncertainties in the location of each measurement and in the location of gradients in the meteorological fields also adversely affect trajectory maps. If a single parcel is initialized in the trajectory model for each measurement, the uncertainty in the location of the advected measurement can increase quite rapidly with time, especially when the parcel is advected through regions of chaotic flow or high wind shear.

To properly assess the magnitude of these errors, both vertical and horizontal positional uncertainties in the location of the measurement need to be considered. The trajectory mapping technique accounts for the two differently. The uncertainty in the horizontal location of an advected measurement can be accounted for by initializing a group of parcels over a region with dimensions on the order of the initial value of that uncertainty. The rate at which each group is sheared apart is then a measure of the rate of growth of that uncertainty.

To determine this rate, 576 "megaparcels" were initialized on the 800 K isentropic surface with a uniform, equal–area distribution poleward of 20° latitude in each hemisphere. Each megaparcel consisted of a central parcel surrounded by four additional parcels (subparcels) located 20 km away on the points of the compass (i.e., one subparcel 20 km east, one 20 km north, etc.). The 40–km megaparcel diameter was chosen to roughly coincide with the width of space over which a single CLAES measurement is made. NMC wind fields were used to advect the parcels for the following two cases: the months of January and June 1992. To prevent contamination of the results by the known low quality of the NMC wind fields in the tropics [*Newman et al.*, 1988], those megaparcels which explored the space equatorward of 15° at any time during the study were discarded.

Figure 1 shows the decrease in the number of compact megaparcels as a function of time for January 1992. A megaparcel is said to be "compact" when all four of the subparcels within it remain within 500 km of the central parcel. Even in the case of the northern winter hemisphere, where the parcel shearing is expected to be largest [*Randel*, 1987b], more than half the megaparcels remained compact for 15–20 days. In fact, in the summer hemisphere the tests indicated that more than half remained compact for the entire month. Because the 800 K potential temperature surface lies close to the jet core in the winter hemisphere, nearly the maxi-

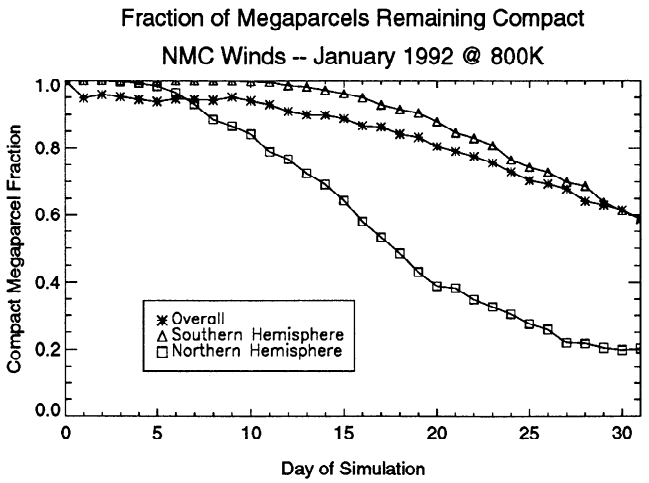

Figure 1. The fraction of compact megaparcels as a function of time. Isentropic trajectories were calculated using National Meteorological Center (NMC) winds during January 1992 on the 800 K potential temperature surface.

mum wind speed gradient is present in these tests. This study, therefore, probably represents a "worst case" scenario.

Some of the shearing distances found in this study were exceptionally large. Nevertheless, the uncertainty in the location of individual advected measurements did not appear to disrupt large–scale spatial gradients in the trajectory maps. The explanation for this behavior appears to be related to the direction in which the shearing uncertainties grow. As the initially tight clusters of parcels were advected forward in time, they tended to remain close together except in regions of high wind shear. In these regions they were pulled apart in a direction parallel to the wind vectors (perpendicular to the gradient in the wind fields). Because this direction is also typically parallel to material and PV isopleths, the accumulation of these positional errors has minimal effect on the structure of the resultant maps. Hence the accuracy of individual trajectories can deteriorate rapidly in this direction without significantly affecting maps of constituent fields.

The initial uncertainty in the vertical location of a measurement affects the accuracy of an isentropic trajectory calculation quite differently. Each parcel is initialized on the isentropic surface of interest, with a constituent value derived from a vertical interpolation of a discrete set of column measurements. Reported errors in measurement of the vertical profile result in uncertainty in the interpolation of this profile. Account of this uncertainty can be kept by initializing each parcel with a constituent value of $\rho \pm \Delta\rho$, where $\Delta\rho$ depends on the magnitude of the vertical gradient of the constituent field and the shape of the isentropic surface at the time and place of the measurement. Unlike the error in the horizontal location, the error $\Delta\rho$ is constant with time.

In summary, the positional uncertainty inherent in satellite measurements can introduce uncertainties in the trajectory mapping technique. Individual trajectory calculations can become inaccurate over short timescales, especially in the presence of large horizontal wind shears. Despite such individual trajectory errors, however, large–scale structures found in trajectory maps appear to be preserved for long periods of time. This phenomenon can be attributed, in part, to the observation that positional uncertainties in parcel location tend to grow in directions parallel to material isopleths, thereby preserving material gradients. These gradients maintain the large–scale structure of the constituent field and promote high field correlations over long periods of time. Disagreements between individual new and old measurements in trajectory maps can often be attributed to the inability of the satellite to detect fine–scale structure in the atmosphere and, therefore, do not necessarily reflect an error in the mapping technique.

4.3 Diabatic Versus Isentropic Calculations

Another inaccuracy in the trajectory mapping technique results from the isentropic approximation. The approximation restricts each trajectory to an isentropic surface under the assumption that each air parcel's potential temperature is conserved along its trajectory. In the atmosphere, diabatic effects cause the potential temperatures of air parcels to change, rendering this approximation inaccurate. These inaccuracies can become particularly important in regions of large vertical wind shear or large vertical constituent gradients. Nevertheless, the isentropic approximation is often employed in trajectory calculations because it significantly reduces computation time.

Regions of large vertical wind shear contribute to errors in isentropic trajectory maps in the following manner. When parcels move off their initial isentropic surface, they encounter somewhat different horizontal winds, both in magnitude and direction. When this difference becomes substantial, the distance between the diabatic and isentropic trajectories grows. To investigate the effects of such errors on individual trajectories and trajectory maps, we examined both the rate at which diabatic and isentropic trajectories separate horizontally and the rate at which this separation causes errors to accumulate in the global constituent fields.

An ensemble consisting of 3480 trajectories was initialized on a uniform, equal–area grid poleward of 20° latitude on the 800 K isentropic surface and advected both diabatically and isentropically. As before, all trajectories which at any time explored the space equatorward of 15° latitude were discarded. Diabatic calculations of the type described by *Schoeberl and Sparling* [1994] were employed.

To evaluate the results quantitatively, we must first define an appropriate measure of the degree of similarity between the trajectories calculated with and without diabatic effects. Any point on the unit sphere can be represented as a unit vector from the origin to that point. A trajectory can then be represented as the curve traced out by the tip of the unit vector as the point moves with time. If we treat the diabatic and isentropic trajecto-

ries in this manner and define their locations at time t by the unit vectors $\hat{x}_d(t)$ and $\hat{x}_a(t)$ respectively, a measure of their separation is then given by the ensemble average

$$< \hat{x}_d(t) \cdot \hat{x}_a(t) >=< \cos\psi(t) > \quad (1)$$

where $\psi(t)$ represents the great circle angular separation between the two trajectories as a function of time. For the case in which the trajectories are completely uncorrelated and the domain is restricted to the space north of latitude ϕ_0 (i.e., given the position of one, the other can be found anywhere in that domain with equal probability), it can be shown that

$$< \cos\psi >= \frac{\cos^4\phi_0}{4(1-\sin\phi_0)^2} \equiv g(\phi_0) \quad (2)$$

Because the diabatic and isentropic trajectories should become uncorrelated in the limit $t \to \infty$, $< \cos\psi(t) >$ should approach $g(\phi_0)$. We define, therefore, a trajectory correlation function by

$$C(t) = \frac{< \cos\psi(t) > - g(\phi_0)}{< \cos\psi(0) > - g(\phi_0)} \quad (3)$$

so that $C(0) = 1$ and $C(\infty) = 0$. As constructed here, $C(t)$ measures the degree to which individual isentropic and diabatic pairs of trajectories are correlated.

We next define a suitable measure of the extent to which fields produced from these two types of trajectories are similar. In order to do this, constituent fields were constructed from the parcel ensembles in the following manner. Each parcel was assigned the value of NMC potential vorticity associated with its initial location (PV_0) to act as a proxy variable for trace gas concentration. Each hemisphere poleward of 15° latitude was divided into a number of equal-area regions, 71 regions for a coarse-scale analysis and 284 regions for a finer-scale analysis. A PV field was then defined at each time by assigning to each region the average value of PV_0 of all parcels contained therein. Although the diabatic ensemble of parcels dispersed vertically, we were not concerned in this study with the specific vertical location of the parcels (the effects of vertical displacement are discussed further below). Rather, we wanted to examine the collective effect on the resultant constituent fields of errors in the horizontal locations of the advected measurements due to the isentropic assumption. As mentioned earlier, the trajectory differences are a consequence of the differences in the horizontal wind fields seen by the diabatic parcels as they rise or descend.

A measure of the degree of similarity between the isentropic and diabatic fields is given by the correlation coefficient

$$r = \frac{\sum_{i=1}^{n}(X_i - \bar{X})(Y_i - \bar{Y})}{\sqrt{\sum_{i=1}^{n}(X_i - \bar{X})^2 \sum_{i=1}^{n}(Y_i - \bar{Y})^2}} \quad (4)$$

where X_i and Y_i are the mean PV_0 values in each of the n regions and $\bar{X}$ and $\bar{Y}$ are the spatially averaged values of PV_0 in the diabatic and isentropic cases respectively. The sum is restricted to those regions for which X_i and $Y_i > 0$.

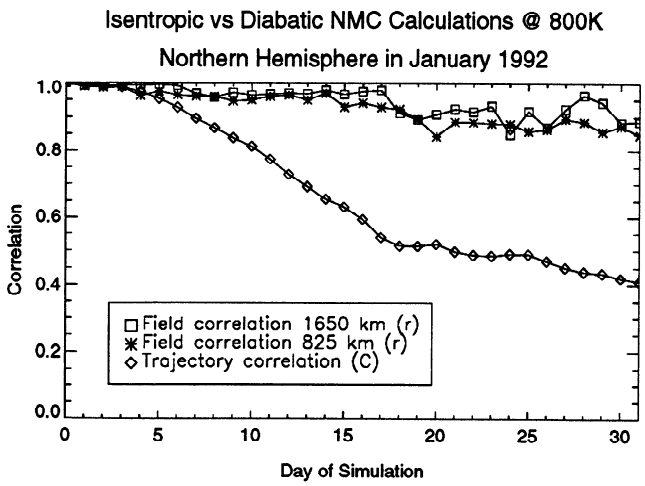

Figure 2a. Statistical analysis of the differences between diabatic and isentropic trajectories and trajectory maps in the northern hemisphere in January 1992.

Figures 2a and 2b show comparisons of the rates at which the field correlation coefficients decay relative to the rates at which individual isentropic and diabatic trajectories become uncorrelated. The calculations were performed in the northern hemisphere in January 1992 and the southern hemisphere in July 1992. In both cases the trajectory correlation decreases to a value of about 0.4 after 31 days. The time evolution clearly shows a residual correlation which persists for long times. The value of the correlation function defined in Equation (3) goes to zero only when the parcels are free to move over the entire domain poleward of 15°. The fact that we observe a nonzero correlation, therefore, indicates that the range of motion of the parcels has been restricted to a smaller domain. In this case the restriction is provided by the transport barrier at the polar vortex edge.

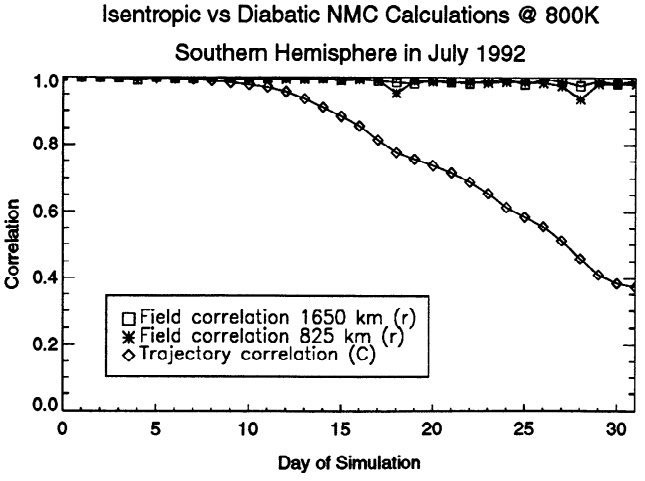

Figure 2b. Same as Figure 2a but for the southern hemisphere in July 1992.

Clear differences in the evolution of the trajectory correlation in the two cases are also evident. The decay is initially much more rapid in the northern winter hemisphere than the Southern winter hemisphere. This difference can be mainly attributed to the difference in wave activity between the two hemispheres, with the northern vortex undergoing more frequent, large-amplitude disturbances than its southern counterpart [*Randel*, 1987b]. On the timescale of this study, it is likely that the small, initial horizontal displacements in the trajectories caused by diabatic effects become amplified in regions of heightened sensitivity to initial conditions.

Despite the relatively rapid growth of errors in individual trajectory calculations, the advected distributions of PV_0 remain highly correlated over the entire period of the study, both at the coarse (1650 km) and fine (825 km) scales. The field correlation is observed to persist for longer times in the southern hemisphere than in the northern hemisphere. This observation can be explained by examining the differences in the vertical dispersion in the two hemispheres.

Figure 3 depicts the mean potential temperature as a function of time for the same ensembles of parcels discussed in Figures 2a and 2b. The error bars represent the 95% confidence limits of the data around the mean. For the heating rates used in this study [*Rosenfield*, 1991], similar average descent rates were found in the northern hemisphere in January 1992 and the southern hemisphere in July 1992. The variance of the potential temperature distribution, however, increases more rapidly with time in the northern hemisphere. The vertical dispersion, rather than the average descent, could be responsible for the larger errors associated with the isentropic assumption in the northern hemisphere. We expect that this vertical dispersion effect will be particularly important if the dynamical features in the horizontal wind fields vary significantly over the range of potential temperatures explored by the diabatic parcels.

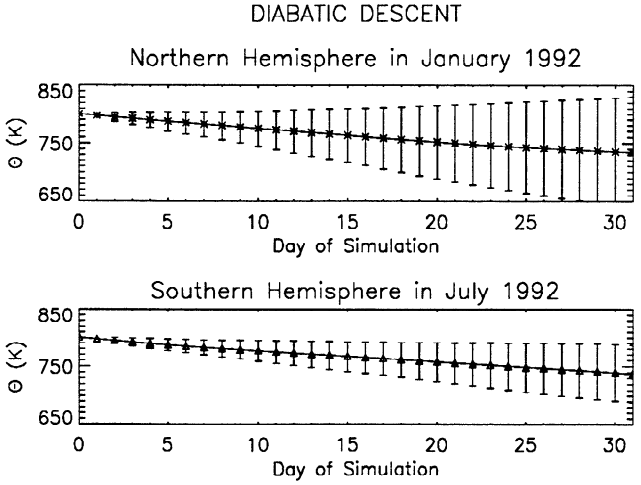

Figure 3. Mean observed descent for the diabatic studies in the winter hemispheres in (top) January and (bottom) July 1992 as calculated from heating rates provided by *Rosenfield* [1991].

If the vertical descent occurs with little dispersion, the isentropic trajectory map may remain an accurate representation of the synoptic field, but one on a lower isentropic surface with time.

Another source of error from the isentropic approximation is related specifically to errors in the vertical location of advected measurements. These errors become important in regions of large vertical constituent gradients. Diabatic motion causes parcels to move vertically across isentropic surfaces. An isentropic trajectory map, therefore, both excludes measurements which have actually been advected to the surface of interest and retains measurements which have actually left the surface. The magnitude of these errors clearly increases with the length of time advected measurements are retained in the map. The rate at which they grow can be estimated by considering the advective flux to the surface. In a manner similar to *Sutton et al.* [1994], we examine the flux given by

$$\dot{\rho} = \left(\frac{dz}{dt}\right)\left(\frac{d\rho}{dz}\right) \tag{5}$$

Since the flux varies across the surface, some features in the trace gas field will be affected more than others.

We estimated this flux for ozone during the periods of January and July 1992, both inside the vortex and at midlatitudes on the 800 K potential temperature surface. For the worst case (January inside the northern polar vortex) the average ozone mixing ratio should have changed by about 30% due to diabatic descent alone over the 31-day period. Changes of roughly 10–24% over the monthlong periods were predicted to result in the other cases. In all cases, changes in the ozone mixing ratio could be limited to less than 10% for isentropic studies confined to periods of about a week. Certainly, the conditions under which trajectory maps are produced (both meteorological and chemical) should be thoroughly understood before trying to interpret the accuracy of the results.

The differences observed between isentropic calculations, diabatic calculations, and calculations using other synoptic mapping techniques are interesting in and of themselves and warrant further study. Comparisons of both diabatically and isentropically advected measurements with nearby, more recent measurements can help assess the amount of heating and/or chemistry associated with a given air parcel. An example of the latter can be found in a recent ozone study using trajectory techniques by *Manney et al.* [1995].

In summary, our statistical analyses show that the isentropic approximation used in most trajectory calculations appears to be valid for individual trajectory calculations of 1 to 2 weeks in length, depending upon the specific meteorological conditions. Information related to the large scale features of the distribution appears to be preserved for even longer periods of time (on the order of 1 month). The actual constituent field, however, may be changing due to vertical motions not captured in the isentropic calculations. While these changes become more significant for constituents with large verti-

cal gradients, the case studies involving ozone indicated changes of less than 10% for calculations of a week or less.

4.4 Sensitivity to Wind Field Analyses

As mentioned earlier, slight displacements of the initial parcel locations near regions of high wind shear can lead to dramatic changes in the subsequent parcel locations. Similarly, a slight displacement of these regions of high wind shear in the wind field analyses can have the same effect. Obviously, large-scale differences in the flow fields will produce large differences in the trace gas fields. Here we examine the sensitivity of trajectory maps to the differences in the location and intensity of smaller-scale wind features. These small-scale differences are likely to be found between different wind field analyses.

To carry out this study, we compared trajectories and trajectory maps produced from the NMC balanced winds [*Newman et al.*, 1988, *Randel*, 1987a] with the assimilated wind analyses produced at the Data Assimilation Office of NASA Goddard Space Flight Center (hereafter referred to as GSFC winds). The study was performed for January and July 1992 in both the northern and southern hemispheres. Again, a distribution of 3480 parcels was initialized on a uniform, equal-area grid poleward of 20° latitude in each hemisphere on the 800 K isentropic surface. Isentropic trajectories were calculated and the resulting maps analyzed with the same two statistical measures outlined in section 4.3. Figures 4a and 4b show the results of these studies.

In Figures 4a and 4b both the trajectory correlation function and the field correlations have been plotted as functions of time for the winter hemisphere. The correlation between the trajectories calculated with different wind fields decays at about the same rate in both hemispheres. This decay rate is much more rapid than was observed in the study assessing diabatic effects. The field correlations, however, remain high for the entire month in both hemispheres, which is to be expected if the wind fields contain basically the same large-scale dynamical information. The fields appear to be somewhat more sensitive to differences in the northern hemisphere, where more numerous small-scale structures provide greater opportunities for differences to arise. The wind field study again suggests that uncertainties in trajectory maps produced from large ensembles of trajectories can often be much smaller than one might expect from the comparatively rapid rate of growth of uncertainty in the individual trajectories.

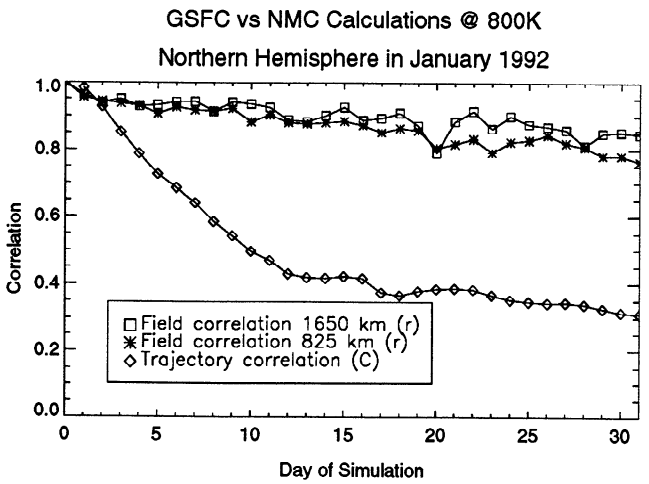

Figure 4a. Statistical analysis of the differences between trajectories and trajectory maps calculated with wind fields from the Data Assimilation Office of NASA Goddard Space Flight Center (GSFC) and those calculated with NMC winds in the northern hemisphere in January 1992.

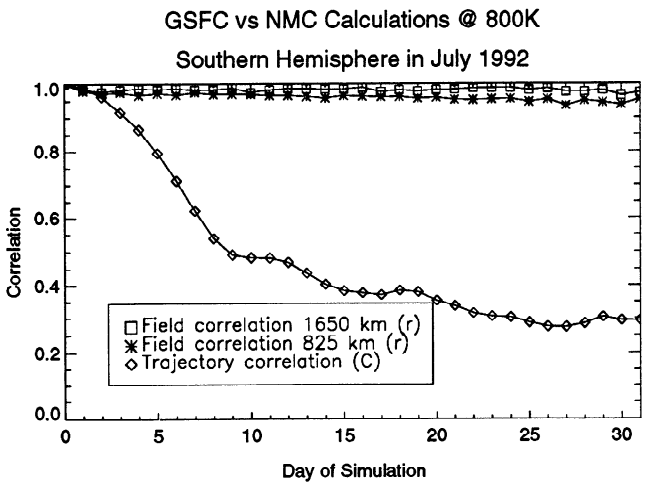

Figure 4b. Same as Figure 4a but for the southern hemisphere in July 1992.

5. Comparison of MLS and HALOE Water Vapor Measurements Using Trajectory Mapping

As a demonstration of the applicability of the trajectory mapping technique to satellite data validation studies, water vapor measurements from MLS (version 3) and HALOE (version 17) were compared. Because MLS and HALOE measurements are not collocated in space or time, the comparison problem is ideally suited for the trajectory mapping technique.

MLS H_2O is available for the southern hemisphere from August 14 through September 21, 1992, and from October 30 through November 28, 1992. Version 3 MLS H_2O is only reliable down to about 46 hPa (22 km) in the stratosphere. Southern hemisphere HALOE measurements are made throughout both of these periods.

The following three separate 1-weeklong periods were selected for this study: August 14–21, September 14–21, and November 1–8, 1992. Comparisons were made for each period on three different potential temperature surfaces: 650 (26 km), 800 (30 km), and 1200 K (38 km).

HALOE's data retrieval pattern restricted the latitude range over which the comparisons were made. For the August period, HALOE measured trace gases be-

Table 1. Restrictions on the Comparison of Microwave Limb Sounder (MLS) and Halogen Occultation Experiment (HALOE) H_2O Data Using Potential Vorticity (PV)

Potential Temperature (K)	Δ PV $\times 10^{-5} \frac{K\ m^2}{kg\ s}$		
	Aug.	Sept.	Nov.
650	2	2	2
800	4	5	4
1200	20	20	20

tween 40° and 60°S latitude. During the September period, HALOE retrieved data between 34° and 54°S. During the November period it gathered data between 25° and 47°S. The August and November HALOE measurements were taken at sunset, while the September HALOE measurements were taken at sunrise.

In order to compare the data sets, trajectory maps were produced for both data sets every 12 hours during each of the three periods. The first appearance of each HALOE H_2O measurement in the HALOE maps was then compared to the average of nearby MLS measurements in the synoptic and concurrent MLS maps. MLS trajectory maps were constructed only from data taken within +/− 1.5 days of the synoptic map time. In this way, errors arising from the trajectory calculations are minimized. To make the comparison with HALOE measurements, MLS data within a 400-km-radius circle (at 800 and 1200 K but 1000 km at 650 K, where fewer reliable MLS H_2O measurements exist) were averaged. To prevent the influence of large, dynamically induced gradients on these averages, Ertel's potential vorticities (calculated from NMC meteorological fields [*Newman et al.*, 1988] and interpolated to each parcel location) were examined. Those MLS parcels with PV values too dissimilar from the PV value associated with the corresponding HALOE measurement were excluded from the averaging calculations. Table 1 shows the PV tolerances used. Finally, only those circles containing more than three advected MLS measurements were included in the study.

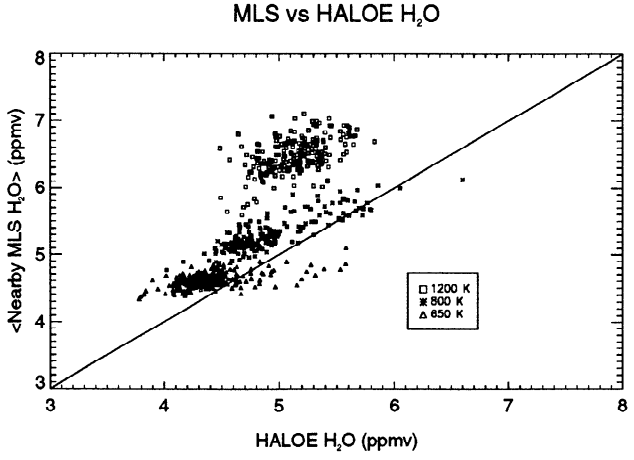

Figure 5. Microwave limb sounder (MLS) (version 3) versus halogen occultation experiment (HALOE) (version 17) H_2O data.

The results of these comparisons are shown in Figure 5 and indicate fairly high correlation between the measurements, with MLS routinely about 0.5 to 1.0 parts per million by volume (ppmv) higher than HALOE and with the highest discrepancies occurring at the highest altitudes. Such results are in good agreement with other validation studies [*Grose*, 1995].

The relative ease with which the comparison of these two noncollocated data sets was made demonstrates the effectiveness and utility of the trajectory mapping technique in satellite data validation studies. Future work will include comparisons of a variety of dissimilar data sets, including both aircraft and satellite measurements.

6. Conclusions

This paper has evaluated both the strengths and weaknesses of the trajectory mapping technique. Studies of N_2O (from CLAES) and H_2O (from MLS) demonstrated the utility and reliability of trajectory mapping. In particular, the technique can produce synoptic maps from asynoptic data, even for periods during which no new data is available (for example, September 10 of Plate 3). The comparison of MLS and HALOE H_2O demonstrated the applicability of the technique to satellite data validation work.

Trajectory maps compare favorably with maps produced using the Salby–Fourier and Kalman filtering methods. All of the gridded synoptic maps agree well with the individual measurements. The nongridded trajectory map, however, allows for a visual estimate of the density and variability of the measurements. Also unlike other techniques, trajectory mapping utilizes knowledge of the wind fields to produce its map products.

Several potential errors in the technique were investigated. The separation between individual trajectories computed with and without diabatic effects grows with time but appears to be small for periods on the order of 7 to 10 days. Changes in the meteorological analyses employed can lead to substantial differences in individual parcel trajectories over much shorter periods (3 days or less). All the studies presented here, however, indicate that trajectory maps (composed of large numbers of advected measurements) remain valid for long periods of time (on the order of weeks). As a result of our error analysis, we strongly caution against the use of a small number of trajectories in examining any chemical or dynamical problem.

The inaccuracies in an isentropic trajectory map which result from neglected diabatic vertical motion are complex and can occur in a variety of ways. In most cases these errors will remain small for studies under 1 week in length. However, we recommend that the meteorological conditions be evaluated before assessing the accuracy of a trajectory map produced in any particular case.

The trajectory mapping technique is a powerful tool with which to analyze satellite data. Future work will

include additional validation studies, an examination of the midlatitude ozone depletion problem, and refinements of the technique itself.

Acknowledgments. This research was conducted under a Global Change Fellowship from the U.S. Department of Energy, administered by Oak Ridge Institute for Science and Education and completed under a National Research Council–NASA Goddard Space Flight Center Research Associateship. Additional funding for the research described in this paper was provided by the EOS Interdisciplinary Science Program and by the NASA Research and Applications Program. Computer resources and funding were provided by the EOS Project. Thanks also go to Arthur Few and Rice University for accommodating this research and to Ricky Rood and the Goddard Data Assimilation Office for supplying the assimilation wind fields.

References

Brasseur, G., and S. Solomon, *Aeronomy of the Middle Atmosphere*, D. Reidel, Norwell, Massachusetts, 1984.

Elson, L.S., and L. Froidevaux, Use of Fourier transforms for asynoptic mapping: Applications to the Upper Atmosphere Research Satellite microwave limb sounder, *J. Geophys. Res., 98*, 23,039–23,049, 1993.

Grose, W.L., and J. Gille (Ed.), Upper Atmosphere Research Satellite Validation Workshop IV report: Temperature and constituents." *NASA Conf. Publ., in press*, 1995.

Haggard, K.V., E.E. Remsberg, W.L. Grose, J.M. Russell III, B.T. Marshall, and G. Lingenfelser, Description of data on the Nimbus 7 LIMS map archival tape. Temperature and geopotential height, *NASA Tech. Pap., 2553*, 1986.

Lait, L.R., and J.L. Stanford, Applications of asynoptic space–time Fourier transform methods to scanning satellite measurements, *J. Atmos. Sci., 45*, 3784–3799, 1988.

Manney, G.L., R.W. Zurek, A. O'Neill, R. Swinbank, J.B. Kumer, J.L. Mergenthaler, and A.E. Roche, Stratospheric warmings during February and March 1993, *Geophys. Res. Lett., 21(9)*, 813–816, 1994.

Manney, G.L., L. Froidevaux, R.W. Zurek, J.W. Waters, A. O'Neill, and R. Swinbank, Lagrangian transport calculations using UARS data, II; Ozone, *J. Atmos. Sci., in press*, 1995.

Newman, P.A., D.J. Lamich, M. Gelman, M.R. Schoeberl, W. Baker, and A.J. Krueger, Meteorological atlas of the southern hemisphere lower stratosphere for August and September 1987, *NASA Tech. Memo., 4049*, 1988.

Pierce, R.B., and T.D.A. Farlie, Chaotic advection in the stratosphere: Implications for the dispersal of chemically perturbed air from the polar vortex, *J. Geophys. Res., 98*, 18,589–18,595, 1993.

Pierce, R.B., W.L. Grose, and J.M. Russell, Evolution of southern hemisphere air masses observed by HALOE, *Geophys. Res. Lett., 21(3)*, 213–216, 1994.

Plumb, R.A., D.W. Waugh, R.J. Atkinson, P.A. Newman, L.R. Lait, M.R. Schoeberl, E.V. Browell, A.J. Simmons, M. Loewenstein, and D.W. Toohey, Intrusions into the lower stratospheric arctic vortex during the winter of 1991/92, *J. Geophys. Res., 99*, 1089–1106, 1994.

Randel, W.J., The evaluation of winds from geopotential height data in the stratosphere, *J. Atmos. Sci., 44*, 3097–3120, 1987a.

Randel, W.J., Global atmospheric circulations statistics, 1000–1 mb." *NCAR Tech. Note NCAR/TN-295+STR*, Natl. Cent. for Atmos. Res., Boulder, CO, 1987b.

Randel, W.J., J.C. Gille, A.E. Roche, J.B. Kumer, J.L. Mergenthaler, J.W. Waters, E.F. Fishbein, and W.A. Lahoz, Planetary wave mixing in the subtropical stratosphere observed in UARS constituent data, *Nature, 365*, 533–535, 1993.

Remsberg, E.E., J.M. Russell, III, L.L. Gordley, J.C. Gille, and P.L. Bailey, Implications of the stratospheric water vapor distribution as determined from the Nimbus 7 LIMS Experiment, *J. Atmos. Sci., 41*, 2934–2945, 1984.

Rosenfield, J. E., A simple parameterization of ozone infrared absorption for atmospheric heating rate calculations, *J. Geophys. Res., 96*, 9065–9074, 1991.

Salby, M.L., Sampling theory for asynoptic satellite observations, I; Space–time spectra, resolution, and aliasing, *J. Atmos. Sci., 39*, 2577–2600, 1982a.

Salby, M.L., Sampling theory for asynoptic satellite observations, II; Fast Fourier synoptic mapping, *J. Atmos. Sci., 39*, 2601–2614, 1982b.

Schoeberl, M.R. and L.R. Lait, Conservative–coordinate transformations for atmospheric measurements, in *Proceedings of the International School of Physics: The Use of EOS for Studies of Atmospheric Physics*, Elsevier Science, New York, 1992.

Schoeberl, M. R. and L. C. Sparling, Trajectory Modelling, in *Diagnostic Tools in Atmospheric Physics, Proceedings of the International School of Physics, Enrico Fermi, Course CXVI*, edited by G. Fiocco and G. Visconti, pp. 289–305, North–Holland, New York, 1995.

Schoeberl, M. R. et al., Reconstruction of the constituent distribution and trends in the Antarctic polar vortex from ER2 flight observations, *J. Geophys. Res., 94*, 16,815–16,845, 1989.

Sutton, R. T., H. MacLean, R. Swinbank, A. O'Neill, and F. W. Taylor, High–resolution stratospheric tracer fields estimated from satellite observations using Lagrangian trajectory calculations, *J. Atmos. Res., 51*, 2995–3005, 1994.

Waugh, D.W., R.A. Plumb, R.J. Atkinson, M.R. Schoeberl, L.R. Lait, P.A. Newman, M. Loewenstein, D.W. Toohey and C.R. Webster, Transport of material out of the stratospheric Arctic vortex by Rossby wave breaking, *J. Geophys. Res., 99*, 1071–1088, 1994.

L. Elson and J. Waters, Jet Propulsion Laboratory, California Institute of Technology, Pasadena, CA 91109–8099.

J. Kumer and A. Roche, Lockheed Palo Alto Research Laboratory, Palo Alto, CA 94304.

L.R. Lait and L.C. Sparling, Hughes STX Corporation, Lanham, MD 20706.

G.A. Morris, P.A. Newman, and M.R. Schoeberl, Code 916, NASA Goddard Space Flight Center, Greenbelt, MD 20771.

J.M. Russell III, Mail Stop 401B, NASA Langley Research Center, Hampton, VA 23681–0001

R.A. Suttie, Heriot–Watt University, Edinburgh, Scotland.

(Received April 12, 1994; revised March 28, 1995;
accepted March 28, 1995.)